Accounting for the Influence of Decorrelation in Microphone Phased Array Deconvolution Methods

Christopher J. Bahr*

NASA Langley Research Center, Hampton, Virginia, 23681

Microphone phased arrays are a common tool for use in aeroacoustic wind tunnel testing. The analysis of acquired array data is known to suffer from decorrelation effects, where the coherence of an acoustic wave measured by a pair of microphones is degraded as the wave passes through a turbulent free shear layer or boundary layer. This paper describes, in detail, how to mitigate the influence of decorrelation effects when processing array data with deconvolution methods. This is done using the Deconvolution Approach for the Mapping of Acoustic Sources (DAMAS) algorithm as an example, applied to recent airframe noise test data acquired in the NASA Langley 14- by 22-Foot Subsonic Tunnel. Two ways of handling the turbulent propagation modeling, both assuming plane wave propagation, are described. Results show that while turbulence model fit parameters may differ, both methods output extremely similar deconvolution results. Further improvements likely require more accurate mean shear layer data prior to developing more involved turbulence models.

Nomenclature

b	=	turbulence-induced correlation function
$\mathbf{C}$	=	cross-spectral matrix
$\mathbf{G}_0$	=	matrix of products of deterministic Green's functions
g_0	=	deterministic Green's function
K_ν	=	order ν modified Bessel function of the second kind
k	=	acoustic wavenumber
$\mathscr{L}$	=	turbulence integral length scale
ℓ	=	source index
N	=	total number of microphones
n	=	microphone index
p	=	acoustic pressure
Q	=	average acoustic source autospectrum
q	=	acoustic source strength
$\mathscr{X}$	=	propagation distance through turbulence
Γ	=	Gamma function
γ	=	mutual coherence function
ρ	=	propagation path separation
σ^2	=	variance of index of refraction
ϕ	=	random phase fluctuations
χ	=	random log-amplitude fluctuations

I. Introduction

Microphone phased arrays are frequently used in aeroacoustic wind tunnel tests to identify, and attempt to quantify, noise sources on aircraft and aircraft component models. However, the beamforming and deconvolution routines used to do this are usually derived assuming deterministic propagation from an acoustic source to the microphones in the array. Under this assumption, the correlation between any pair of microphones in the array is perfect when observing an isolated plane wave or point source, yielding unit coherence for frequency-domain analyses. In practice, the acoustic

wave from a given source passes through a turbulent boundary layer in closed wall facilities and a turbulent free shear layer in open-jet facilities. Propagation through turbulence is known to decorrelate the acoustic field observed by arrays, leading to a degradation in the performance of conventional analysis routines [1–4]. The extent of this decorrelation is dependent on microphone layout and turbulence characteristics, and it has been shown to be stronger for free shear layers when compared to wall-bounded flows for equivalent test section conditions [5].

Recently, there have been efforts to mitigate the impact of decorrelation on traditional array processing methods. These have been formulated both in terms of a level correction for integrated spectra determined using conventional beamforming [6], and in terms of a point-by-point correction using a deconvolution technique [7]. The latter of these is expounded upon in this work, and was introduced briefly as part of a broader effort in studying the High-Lift Common Research Model (CRM-HL) in the NASA Langley Research Center 14- by 22-Foot Subsonic Tunnel (14x22) [8]. The overall test campaign is documented in several companion papers that address background noise mitigation in the 14x22 [9], slat noise characterization of the CRM-HL [10], development and assessment of slat noise reduction concepts [11], and comparison of experimental and simulated results [12]. This work develops the deconvolution correction technique in more detail using a plane wave model with two different propagation models, and shows its application to CRM-HL data using the Deconvolution Approach for the Mapping of Acoustic Sources (DAMAS) algorithm [13].

II. Propagation in Random Media

Beamforming and deconvolution methods require modeling the propagation from a source of interest to an array of microphones, as illustrated in Fig. 1. The source of strength q is assumed to exist at location ℓ. A Green's function g is chosen as an assumed model for propagation to an N element microphone array. For a given frequency (notation suppressed), the pressure at microphone n due to the source at ℓ is expressed as

$$p_{n,\ell} = g_{n,\ell} q_\ell. \tag{1}$$

In aeroacoustic applications, q_ℓ is often a random variable, so the auto- and cross-spectra computed from the microphone array are used rather than the pressure. Within a scaling factor, depending on whether one- or two-sided spectra or spectral densities are desired, these are found by ensemble averaging the outer product of the column vector of microphone measurements $\mathbf{p}_\ell$ with its conjugate transpose $\mathbf{p}_\ell^\dagger$,

$$\mathbf{C}_\ell = \left\langle \mathbf{p}_\ell \mathbf{p}_\ell^\dagger \right\rangle = \left\langle \mathbf{g}_\ell q_\ell q_\ell^* \mathbf{g}_\ell^\dagger \right\rangle. \tag{2}$$

Under deterministic propagation conditions, vectors $\mathbf{g}_\ell$ and $\mathbf{g}_\ell^*$ are constant and factor out of the ensemble averaging operation. The resultant cross-spectral matrix, or CSM, is then the rank 1 outer product of the vectors of Green's functions multiplied by the autospectrum of the source,

$$\mathbf{C}_{0\ell} = \mathbf{g}_{0\ell} \mathbf{g}_{0\ell}^\dagger \left\langle q_\ell q_\ell^* \right\rangle = \mathbf{G}_{0\ell} Q_\ell. \tag{3}$$

Matrix $\mathbf{G}_{0\ell}$ models the propagation component of $\mathbf{C}_{0\ell}$, and is used by DAMAS and other deconvolution routines to fit distributions of acoustic sources to measured data.

When propagation is not deterministic, simplifying the expected value operation in Eq. (2) requires more effort. By expressing each term as the sum of mean and fluctuating components and assuming that the fluctuating components of the propagation terms are uncorrelated with the fluctuating components of the source signal, it can be shown that

$$\left\langle \mathbf{g}_\ell q_\ell q_\ell^* \mathbf{g}_\ell^\dagger \right\rangle = \left\langle \mathbf{g}_\ell \mathbf{g}_\ell^\dagger \right\rangle Q_\ell. \tag{4}$$

The propagation element to microphone n can be expressed in terms of the deterministic propagation component to the microphone $g_{0n,\ell}$, phase fluctuations $\phi_{n,\ell}$, and log-amplitude fluctuations $\chi_{n,\ell}$ [14], giving

$$g_{n,\ell} = g_{0n,\ell} e^{j\phi_{n,\ell} + \chi_{n,\ell}}. \tag{5}$$

Substituting Eq. (5) into Eq. (4) and using Eq. (2), an element of the modeled CSM is then given as

$$C_{n,n',\ell} = g_{0n,\ell} g_{0n',\ell}^* \left\langle e^{j(\phi_{n,\ell} - \phi_{n',\ell}) + \chi_{n,\ell} + \chi_{n',\ell}} \right\rangle Q_\ell. \tag{6}$$

The complex exponential term inside the ensemble averaging operation in Eq. (6) acts to reduce the coherence between microphones n and n', and can be expressed as a mutual coherence function, or MCF, $\gamma_{n,n',\ell}$. The overall model CSM is thus given as the Hadamard product of the deterministic propagation matrix and the matrix of MCF values [15],

$$\mathbf{C}_\ell = \left(\mathbf{G}_{0\ell} \odot \boldsymbol{\gamma}_\ell \right) Q_\ell. \tag{7}$$
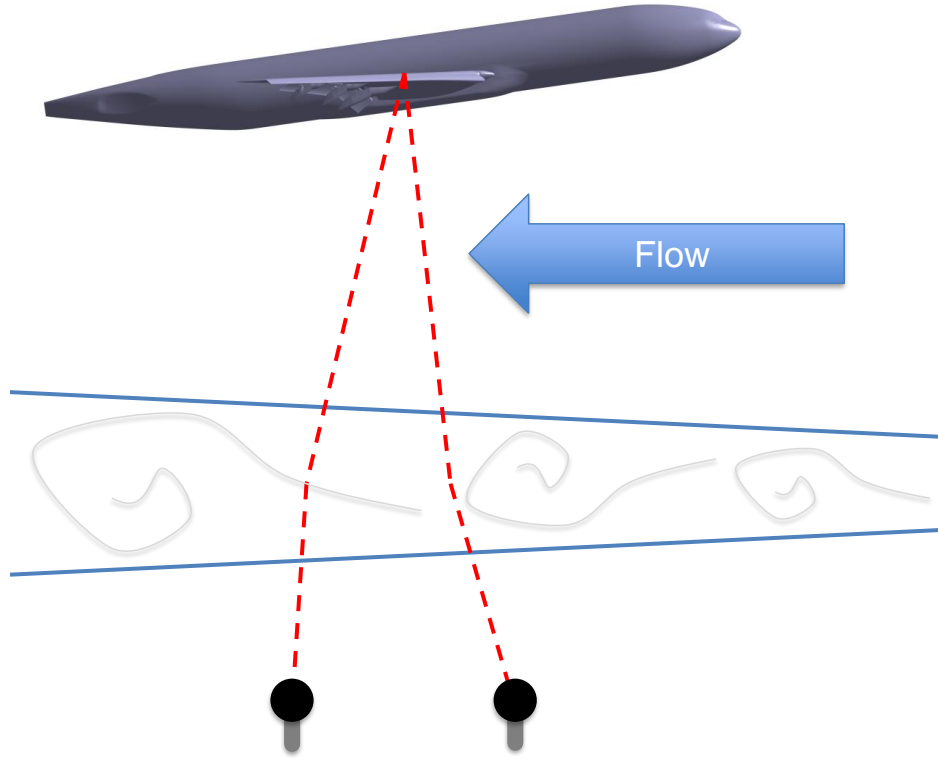
Fig. 1 Schematic of propagation from an airframe noise source to a pair of array microphones in an open-jet wind tunnel facility. Sound passes through the turbulent free shear layer that bounds the test section core flow and the nominally quiescent surroundings.

The propagation and MCF matrix components of the model CSM are subsequently used, in the case of DAMAS, to generate the coefficient matrix required for the deconvolution process [7].

III. Determining Coherence Loss

To incorporate coherence loss effects into a deconvolution routine, matrix γ_ℓ must be generated for every candidate source location. In this work, this is done by first selecting a model for the MCF, and then using an acoustic source to determine best-fit model parameters.

A. Coherence loss model

Unless coherence loss can be measured from every source location of interest at every frequency of interest, a model for the MCF must be used. Wilson [15] gives a general form for $\gamma_{n,n',\ell}$, assuming plane waves, as

$$\gamma_{n,n',\ell} = \gamma\left(\rho_{n,n'}, \mathscr{X}_\ell\right) = e^{-\frac{\pi}{2}k^2 \mathscr{X}_\ell \left[b(0) - b(\rho_{n,n'})\right]}. \tag{8}$$

This model is based on the parabolic wave equation and the Markov approximation. In Fig. 1, the direction of propagation for the parabolic simplification can be taken as normal to the flow direction. The distance an acoustic wave propagates through the turbulent free shear layer in this direction is given by $\mathscr{X}_\ell$. The separation between microphones n and n' in the plane normal to the direction of $\mathscr{X}_\ell$, as used in the Markov approximation, is $\rho_{n,n'}$. The acoustic wavenumber is

given by k and b is a 2-D correlation function. It is further assumed that propagation occurs through homogeneous, isotropic, and nonintermittent turbulence. The reader should note that every one of these assumptions is violated in a large open-jet wind tunnel facility.

Wilson defines correlation functions for several models of turbulence spectra. Of those given, the von Kármán correlation function provides the best fit to the data acquired in the 14x22 test, and is used here. It is given by

$$b\left(\rho_{n,n'}\right) = \frac{4\sigma^2 \mathscr{L}}{3\sqrt{\pi}\Gamma\left(\frac{1}{3}\right)} \left(\frac{\rho_{n,n'}}{2\mathscr{L}}\right)^{\frac{5}{6}} \left[K_{\frac{5}{6}}\left(\frac{\rho_{n,n'}}{\mathscr{L}}\right) - \frac{\rho_{n,n'}}{2\mathscr{L}}K_{\frac{1}{6}}\left(\frac{\rho_{n,n'}}{\mathscr{L}}\right)\right]. \tag{9}$$

Here, Γ is the Gamma function and K_ν is the order ν modified Bessel function of the second kind. The term σ^2 is related to the variance in index of refraction and scales with the square of the free stream Mach number [1]. In this formulation it is nondimensional. $\mathscr{L}$ is an integral length scale related to the size of the turbulent eddies, and matches the units of $\rho_{n,n'}$. Note that for very small values of $\rho_{n,n'}$ an alternate asymptotic form of this equation may be required for computation,

$$\lim_{\rho_{n,n'}\to 0} b\left(\rho_{n,n'}\right) \approx \frac{2\sigma^2 \mathscr{L}}{3\sqrt{\pi}\Gamma\left(\frac{1}{3}\right)} \left[\Gamma\left(\frac{5}{6}\right) - \Gamma\left(\frac{1}{6}\right)\left(\frac{\rho_{n,n'}}{2\mathscr{L}}\right)^{\frac{5}{3}}\right]. \tag{10}$$

With these equations, if σ and $\mathscr{L}$ can be determined for a given experimental condition, the MCF can be computed. However, in many situations, it may be impractical to acquire high quality measurements of turbulence characteristics. In large scale tunnels in particular, the equipment required to acquire such data while surviving the abuse of an industrial scale free shear layer are likely expensive and intrusive, with installation requirements beyond both the monetary and schedule budgets of many aeroacoustic tests.

B. Coherence loss measurement

For tests where the above circumstances hold, an alternative approach exists. Measure the MCF for a given source location ℓ, find optimum values for σ and $\mathscr{L}$ to fit the von Kármán MCF to acquired data, and then use an estimate of the mean shear layer profile to generalize the MCF from a source at ℓ to candidate source locations at ℓ'.

Consider a minimally-intrusive acoustic source installed in the wind tunnel of interest. This may take the form of a speaker embedded in a model [8], or possibly as a laser-induced plasma [5]. The laser provides a deterministic acoustic waveform, while the speaker can provide either deterministic or bandlimited random signals. The following assumptions are made:

- A single, dominant acoustic source is operated. The source must be loud enough that other acoustic sources and/or other forms of microphone contamination have a small effect on a coherence calculation. CSM background subtraction may help with this [16].
- Source directivity does not have a significant influence on computed coherence, e.g., no microphones are located near a directivity null.
- The source is sufficiently small such that it is adequately modeled as being confined to location ℓ and appears compact with respect to a coherence calculation [17].
- Propagation from the source to each microphone occurs along a single path, e.g., there are no significant reflections within the wind tunnel test section.

Under these assumptions, the MCF for all microphone pairs at all frequencies should be unity under ideal, deterministic propagation conditions. This means that the measured coherence for every microphone pair, if not unity, is reduced due to fluctuations in the propagation path.

The MCF can be estimated from the measured CSM, $\hat{\mathbf{C}}$, using the usual definition of the coherence function,

$$\hat{\gamma}_{n,n',\ell} = \sqrt{\frac{\hat{C_{n,n',\ell}}\hat{C_{n',n,\ell}}}{\hat{C_{n,n,\ell}}\hat{C_{n',n',\ell}}}}. \tag{11}$$

Substituting Eq. (6), simplifying, and assuming that $\gamma_{n,n',\ell}$ is a positive real value per Eq. (8) yields

$$\hat{\gamma}_{n,n',\ell} = \frac{\left\langle e^{j\left(\phi_{n,\ell}-\phi_{n',\ell}\right)+\chi_{n,\ell}+\chi_{n',\ell}}\right\rangle}{\left\langle e^{\chi_{n,\ell}}\right\rangle\left\langle e^{\chi_{n',\ell}}\right\rangle}. \tag{12}$$

4

Under the weak scattering assumption, where time delay fluctuations will be the dominant source of variation (corresponding to phase variation in the frequency domain), the denominator of Eq. (12) is unity and $\hat{\gamma}_{n,n',\ell} = \gamma_{n,n',\ell}$. However, acoustic propagation through an open-jet test section free shear layer has been observed to experience strong scattering [5]. This means that the computed coherence estimate from Eq. (11) does not equal the MCF. Assumptions about the nature of the magnitude fluctuations, e.g., χ is a Gaussian random variable, allow further simplification. However, they do not clearly cancel the denominator term in Eq. (12), and so are not pursued further. It is assumed that any offset introduced by strong scattering to the MCF calculation is not significant for the application presented in this work.

With a measured estimate of the MCF from Eq. (11) for every pair of microphones in the array, a curve fit to Eq. (8) can now be performed to find optimal, frequency independent values of σ and $\mathscr{L}$ using all the coherence data for all valid frequencies. Performing the fit requires knowing $\mathscr{X}_\ell$, or the portion of the acoustic propagation path that passes through the turbulent free shear layer. This returns to the problem of a test requiring a map of the facility flow field. However, determining the mean shape of the test section shear layer is easier than measuring turbulence characteristics. In the author's experience, facilities are far more likely to have historical data on the mean flow characteristics of the test section than detailed maps of turbulence characteristics in shear layers. An estimate of the shear layer thickness can be used in conjunction with a shear layer intersection calculation [18], so an approximate path through the shear layer can be computed for each microphone. Once this is done, determining σ and $\mathscr{L}$ is a straightforward optimization problem. The MCF for points $\ell' \neq \ell$ can then be determined by computing $\mathscr{X}_{\ell'}$, and Eq. (7) can be used to modify the DAMAS coefficient matrix.

It should be noted that there are multiple ways to implement the turbulent coherence loss model, and these will yield different fit parameters when used with a calibration source. One way is to set $\mathscr{X}_\ell$ to the total path length through the turbulent free shear layer, herein taken at the 2.5% and 97.5% points of the normalized velocity profile, and specify the physical microphone separation as $\rho_{n,n'}$. This was described by Ernst et al. [3] and used in the initial version of the 14x22 data analysis [7], with the additional assumption that a single $\mathscr{X}_\ell$ value, the distance from the calibration source to the array center, was sufficient to correct the data. This implementation is illustrated in Fig. 2a.
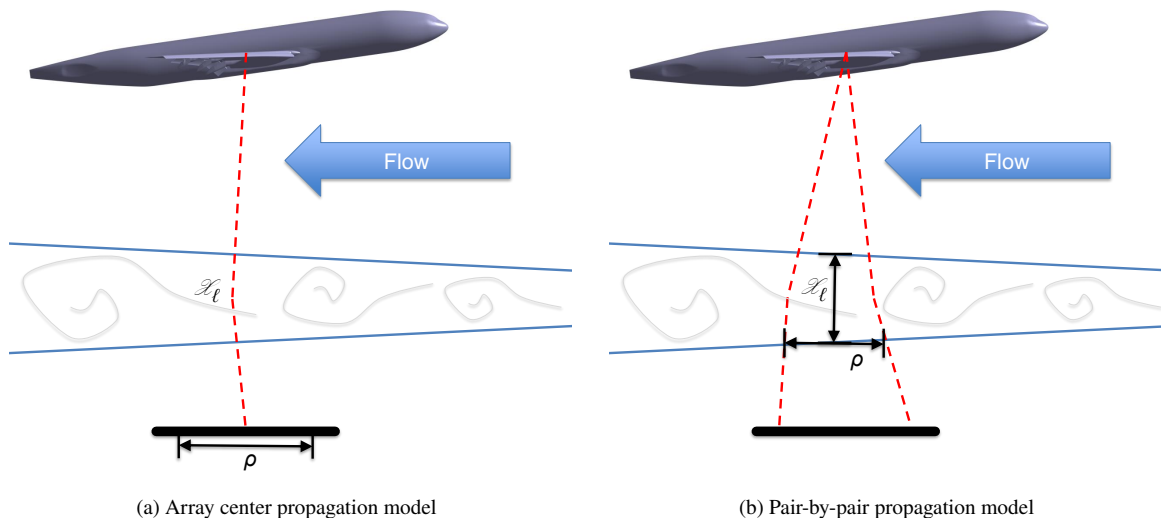

(a) Array center propagation model   (b) Pair-by-pair propagation model

Fig. 2   Comparison of the two propagation models used to determine turbulence parameters.

A second implementation, illustrated in Fig. 2b, can also be constructed. This method more closely follows the derivations provided by Ostashev and Wilson [19]. Here, $\mathscr{X}_\ell$ strictly follows the propagation direction of the parabolic assumption, with the understanding that small deviations from this direction are allowable with the parabolic wave equation. Per the reference, a layered media approach is taken where layers with different turbulence characteristics can be analyzed sequentially. In this case, $\mathscr{X}_\ell$ is then determined by averaging the shear layer entry and exit points when tracing two propagation paths through the shear layer, and computing the flow-normal distance between those

two points. The distance $\rho_{n,n'}$ is taken as the planar path separation at the average exit point. This method handles microphones on a pair-by-pair basis, rather than as a whole array. While it has more geometric parameters to track, it allows the turbulence model to account for the thickening shear layer seen by downstream pairs of microphones.

Both of these implementations are designed for propagation through a planar shear layer, where propagation from the source to the array is within a limited range of angles according to the parabolic wave equation. They do not account for wide angle propagation, nor do they account for shear layer curvature introduced by the presence of a lifting model or other facility effects. Due to these and other limitations, there should be no expectation that either propagation model will yield σ or $\mathscr{L}$ values that would match detailed measurements of the turbulent free shear layer.

IV. Test Description and Data Processing

Various details of the acoustic test configuration can be found in companion publications for this work [7–12]. The most relevant information is repeated here. The CRM-HL was tested in the 14x22 open-jet configuration in 2020/2021. A traversing array of 97 1/4-inch (6.35-mm) microphones was installed in the facility and is shown with the CRM-HL in Fig. 3. This array had been designed for previous open-jet tests in the 14x22 [20]. For this test, the center of the array face was located 1.83 m off the floor and 5.17 m from the test section centerline. The array could be traversed from upstream locations (small angles) to downstream locations (large angles), with 90° locating the array at the same streamwise location as the CRM-HL center of rotation, which is close to the center of the wing.
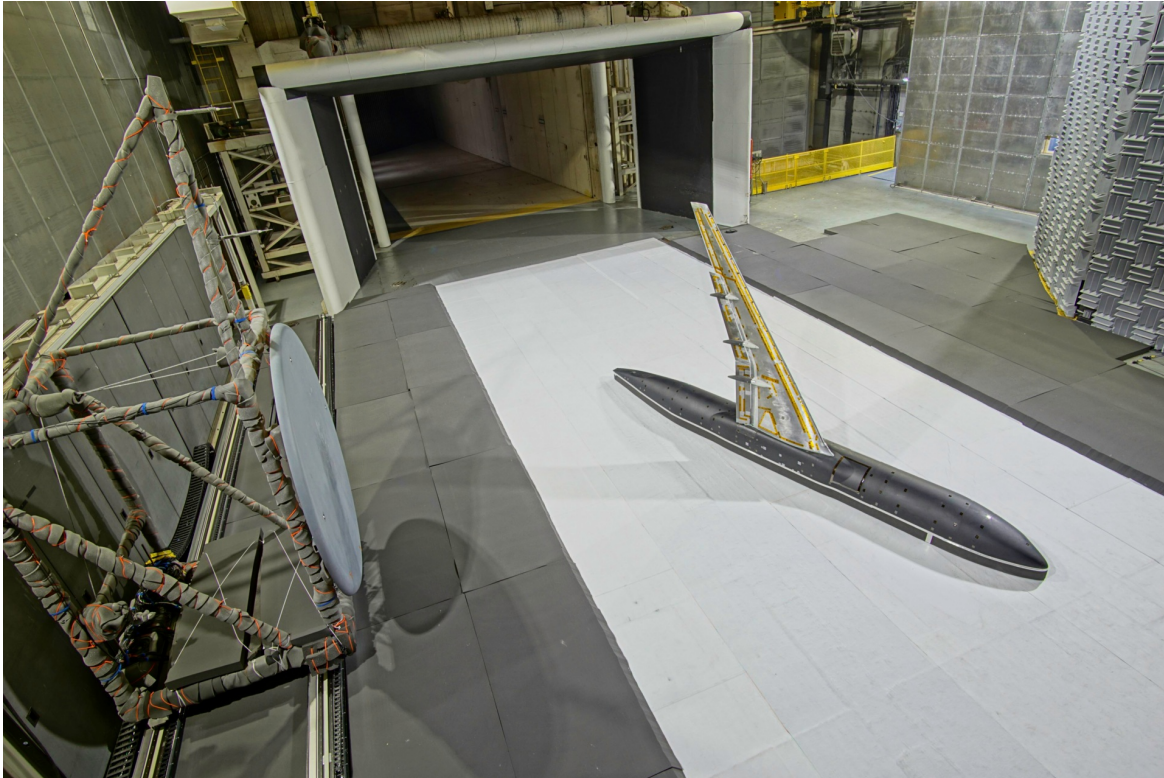

Fig. 3 **Traversing microphone array and CRM-HL model in the open-jet configuration of the 14x22.**

Array data were acquired at a sampling rate of 196,608 samples/sec for 35 seconds at every test condition. In this work, spectra were computed using block lengths of 2,048 samples, yielding a narrowband binwidth of 96 Hz. Blocks were processed with a Hann window and 75% overlap. Prior to any beamforming or deconvolution analysis, subspace-based background subtraction was performed using empty tunnel data for matching flow conditions and array locations [16]. Conventional beamforming steering vectors were selected such that the array response would have a maximum at an isolated point source [7, 21]. The array shading scheme was optimized to hold the array response 3-dB beamwidth to 22.5 cm across the majority of the frequency range of interest, with a controlled increase in beamwidth at lower frequencies [22]. The beamforming and deconvolution grid was selected to encompass the wing section of the
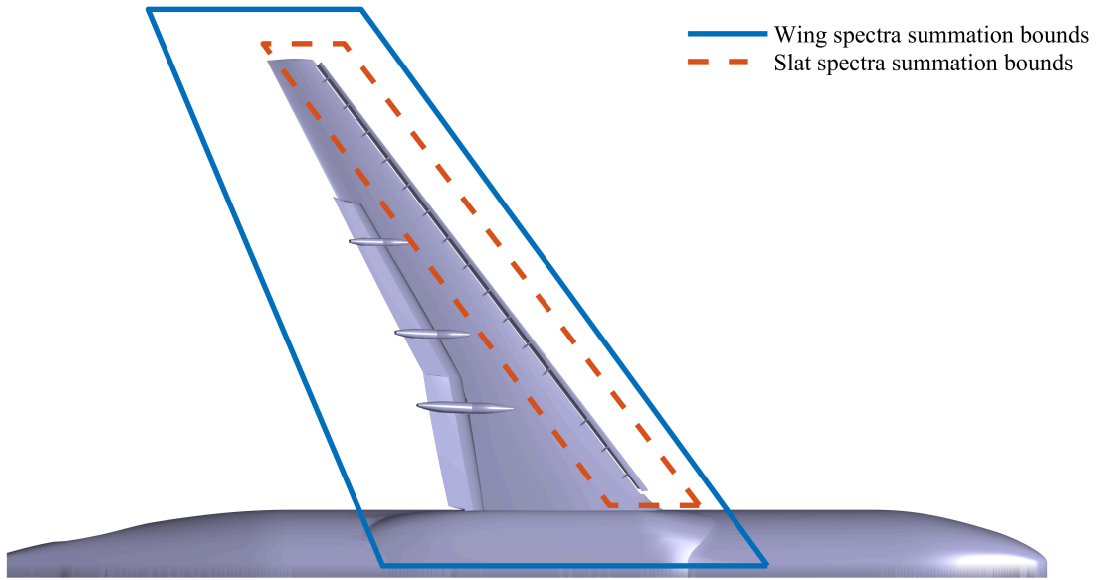
Fig. 4   Overlay of summed spectra regions with the CRM-HL model.

model, spanning approximately 4 m in the streamwise direction and 5 m in the flow normal direction, with 1 m extended into the floor to capture model-induced noise sources that appeared on the floor for portions of the test [8]. The grid point spacing was 4.5 cm, yielding 5 points per beamwidth and 10,080 grid points. For each test condition, the grid was rotated to match the model dihedral and angle of attack.

The deterministic propagation model used in the DAMAS algorithm was based on a point source solution for propagation through a free shear layer modeled as a planar interface, with both magnitude and phase corrections selected to give an equivalent source level at the array center emission location [13, 18]. Atmospheric attenuation [23] and microphone directivity [24] were incorporated into the propagation model to estimate lossless deconvolution output corrected for installation effects. The DAMAS algorithm was applied using 200 forward-backward iterations following four different grid traversing orders. While in previous work a 6 dB correction was subtracted from the DAMAS output to account for pressure doubling on the array face when comparing facility configurations with projected spectra [7], this was not done here. For summed spectra, two regions are defined. One encompasses the whole model wing, and the other the isolated slat. These are shown in Fig. 4.

V. Mutual Coherence Function Fits

A wing-embedded speaker in the CRM-HL was used to generate signals for the MCF estimation. Band-limited random signals were fed through the speaker in five approximate octave bands spanning from 1.4 kHz to 42 kHz. The approach was chosen as a trade-off between maximizing speaker output at a given frequency and limiting the number of acquisitions added to the overall test matrix. It was observed that reflections from the tunnel floor treatment were strong enough to interfere with MCF calculations below 9 kHz. Above 36 kHz, the signal-to-noise ratio was insufficient at higher Mach numbers. Thus, the coherence data from 9 kHz to 36 kHz were used to determine σ and $\mathcal{L}$. Note that for some run conditions, the model generated strong slat tones. The coherence data at these frequencies were also excluded from the fitting process. Best fit values for these parameters were computed for most combinations of Mach number, array traverse station, and model angle of attack of interest. The model angle of attack was included in case the change in aerodynamic interaction between the model lift and free shear layer characteristics altered the behavior of the shear layer turbulence. However, in the fitting process it was found that model angle of attack did not have a significant influence on the fit parameters.

Sample fits of the MCF models to speaker coherence data are shown in Figs. 5 and 6. These plots overlay the best fit
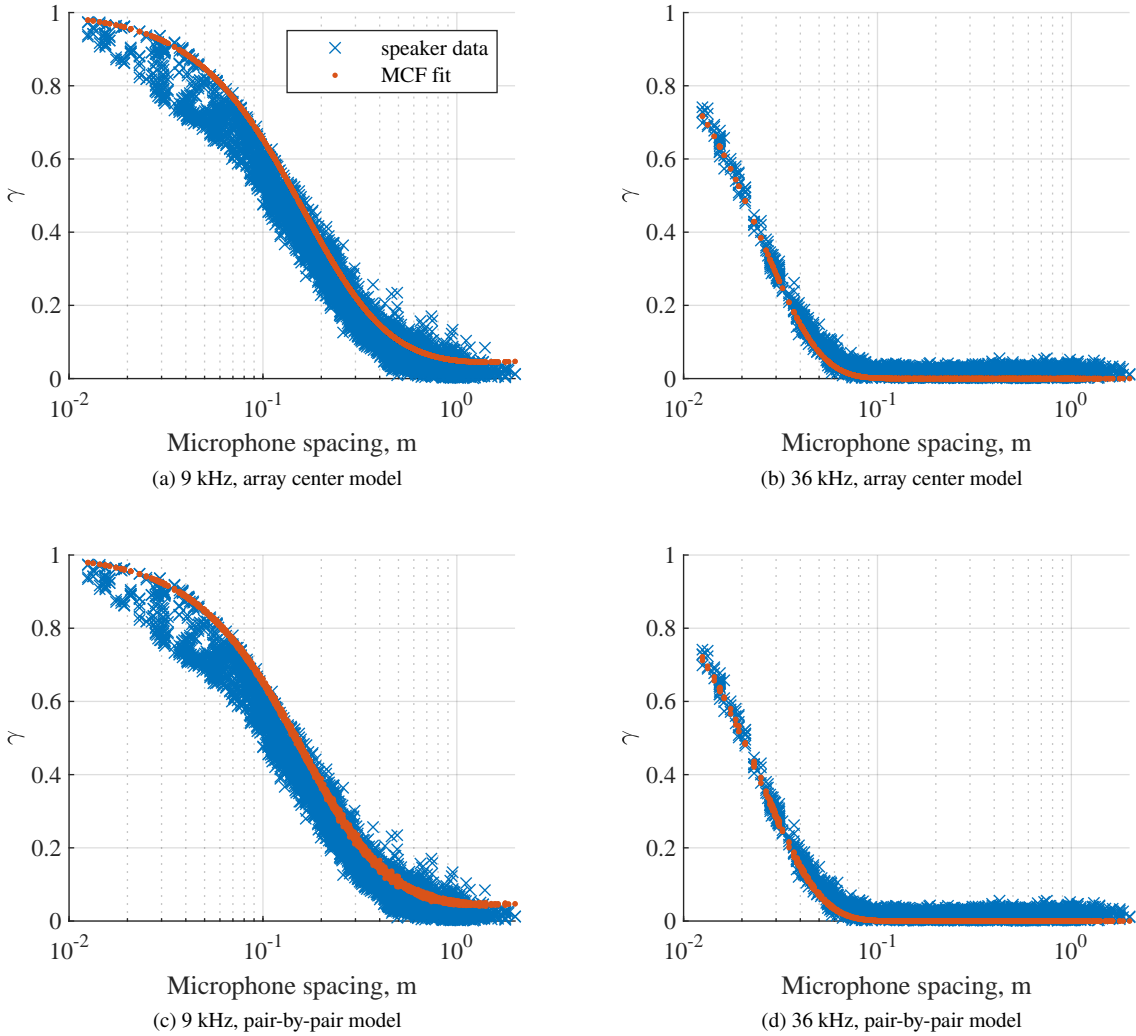
(a) 9 kHz, array center model

(b) 36 kHz, array center model

(c) 9 kHz, pair-by-pair model

(d) 36 kHz, pair-by-pair model

Fig. 5 **Comparison of MCF fits between the two considered propagation models. Results are for Mach 0.16 at the 90° array station and 8.5° angle of attack. For the array center model, $\sigma = 0.028$ and $\mathcal{L} = 0.42$ m. For the pair-by-pair model, $\sigma = 0.033$ and $\mathcal{L} = 0.32$ m.**

models to the coherence values of all 4,656 unique pairings of microphones as a function of microphone spacing. In both figures, the first row of subfigures shows the MCF fit for the array center propagation model, and the second row shows the fit for the pair-by-pair propagation model. The first column shows the fit at the lower bound of the fitting data range, 9 kHz, and the second column shows the fit at the upper bound of the fitting data range, 36 kHz. Note that these plots show the coherence as a function of microphone spacing for both propagation models rather than ρ, as ρ varies for a given pair of microphones depending on the propagation model selection.

The results for the 90° array station, shown in Fig. 5, are examples of good model fits. At both frequencies, both models capture the data trends. The fit of the pair-by-pair model is multivalued when plotted with respect to microphone spacing, as microphone pairs with the same spacing can have different ρ and $\mathcal{X}_\ell$ values. However, allowing for these to vary in the model does little to account for the full data spread, and the overall coherence behavior is extremely similar between the models even though the fit parameters are different.

The results for the 70° array station, shown in Fig. 6, are examples of the model fit struggling with reduced data quality. While the models capture the data trends at 36 kHz, at 9 kHz they fail to match the data behavior at larger microphone spacings (though this poor fit is somewhat mitigated in beamforming and deconvolution by the array shading
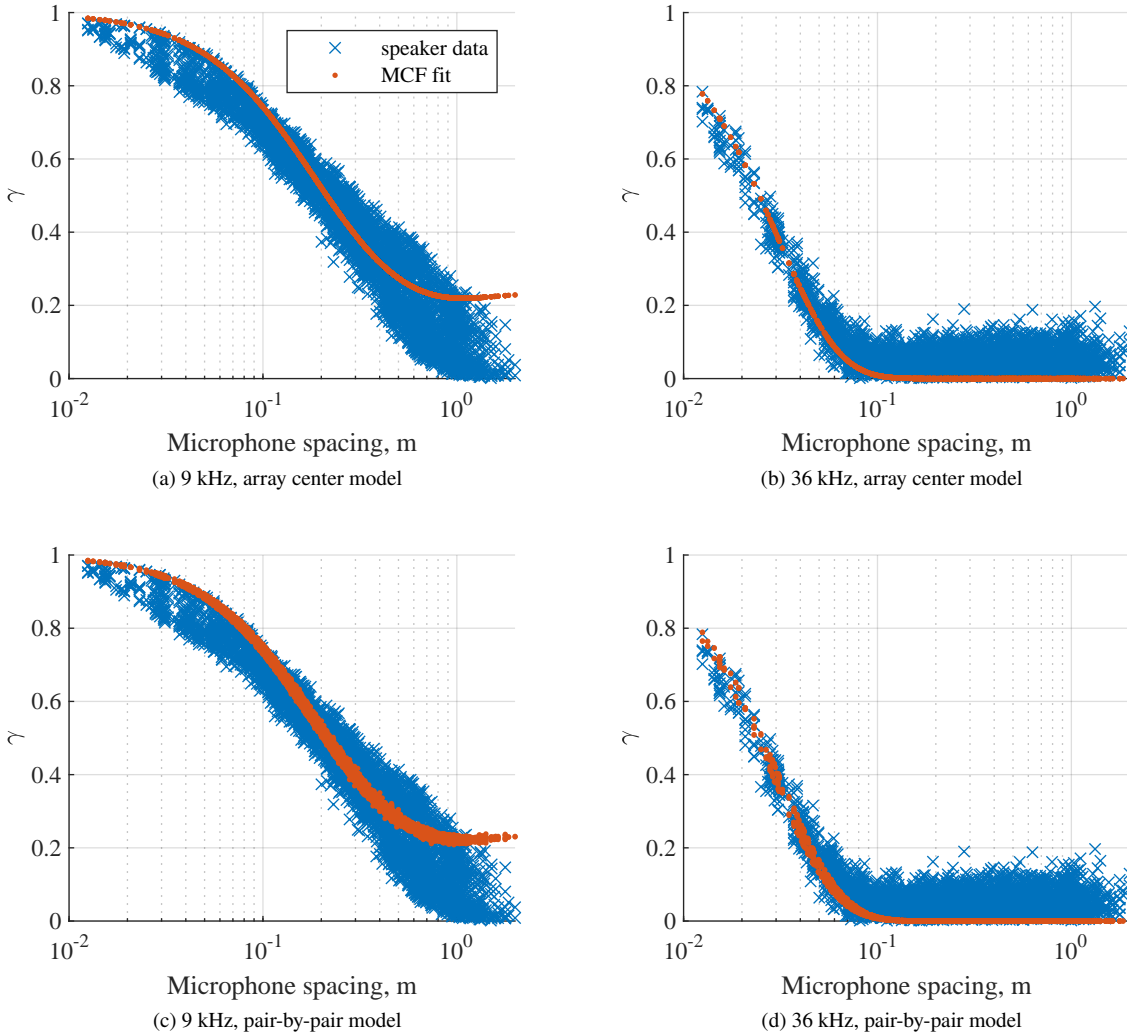
(a) 9 kHz, array center model

(b) 36 kHz, array center model

(c) 9 kHz, pair-by-pair model

(d) 36 kHz, pair-by-pair model

Fig. 6   Comparison of MCF fits between the two considered propagation models. Results are for Mach 0.16 at the 70° array station and 8.5° angle of attack. For the array center model, $\sigma = 0.023$ and $\mathscr{L} = 0.32$ m. For the pair-by-pair model, $\sigma = 0.029$ and $\mathscr{L} = 0.22$ m.

function). The multivalued behavior of the pair-by-pair model is greater at 70° than at 90°. The more oblique look angle from the source to the array leads to more spread in ρ and $\mathscr{X}_\ell$ values when compared to the near-normal incidence of 90°. However, this increased multivalued spread still does little to cover the measured range of coherences for a given microphone spacing. As with the 90° data, the 70° data show extremely similar behavior between the two models.

VI. Deconvolution Results

DAMAS outputs for the 90° array station are shown in Fig. 7. These results are for a full-span slat model condition, with Mach numbers, array station, and angle of attack matched to the conditions for the example coherence plots in Fig. 5. The exact model slat configuration is one that was evaluated in both the 2018 and 2020/2021 wind tunnel tests [7], and is considered here to allow some traceability with respect to the development of analysis techniques. This configuration does not match the one studied in companion analysis of the phased array characterization of the model slat noise radiation [10].

For reference, the output from the baseline DAMAS algorithm, not accounting for decorrelation, is given in the first row of subfigures. The second and third rows are the array center model and pair-by-pair model, respectively. The

first column shows results for the 5 kHz one-twelfth octave band, giving an example of data outside the model fitting frequency range. The second column shows results for the 20 kHz one-twelfth octave band, giving an example of data within the fitting range. As expected, ignoring decorrelation effects in deconvolution produces results that are of limited use. Noise is mapped to the overall wing, but the maps are smeared such that attempting to isolate a more refined source region for level calculations is nearly impossible at higher frequencies. The two different turbulence propagation models yield extremely similar deconvolution maps, with only minor differences in peak levels and source distributions. Both models assign noise sources to the expected locations on the slat, flap brackets, and flap side edges. Some displacement of sources from the model is apparent, and most evident near the tip of the wing.

DAMAS outputs for the same configuration and run conditions, without the baseline comparison, are shown at the 70° array station in Fig. 8 and at the 110° array station in Fig. 9. These different directivity results show the same overall behavior as the 90° data. There is very little difference between results using the two turbulence propagation models, though the 70° data show a bit more variation in map peak levels at 20 kHz. Source displacements behave in a similar fashion, most evident near the wing tip but also present near the model fuselage. Notably, the displacement shows some frequency dependence at the 110° array station.

In an attempt to further evaluate this displacement, the results for Mach 0.12 are shown in Fig. 10, and for Mach 0.20 in Fig. 11. Both of these are for the 90° array station and show similar overall displacement trends, though the scales of the displacement may differ. Displacement is difficult to assess at high frequencies for the Mach 0.20 data, as the intense noise source near the inboard portion of the slat overwhelms any other sources that might be present.

It is difficult to tell if this source shifting is due to the turbulent propagation models or some other effect. The 5 kHz data in the baseline DAMAS results of Fig. 7a may show a mild source shift near the wing tip, but the 20 kHz map of Fig. 7b is too smeared to see anything useful. However, it is known that curvature in real wind tunnel shear layers will yield incorrect propagation time calculations when using Amiet's planar shear layer correction [25, 26]. For this particular test, empty tunnel shear layer measurements and a planar assumption are being applied to a shear layer that is being deflected by a semispan aircraft model with high lift rigging and variable loading across the wingspan. The shear layer is not planar. Without a more accurate estimate of the mean shear layer behavior and associated deterministic propagation delays, no attempt can be made to assess possible source map shifts due to turbulent propagation modeling.

Summed region spectra are shown as a function of array measurement station in Fig. 12 and as a function of Mach number in Fig. 13, comparing the behavior for both turbulent propagation models. Note that the source summation bounds are set large enough to account for most of the aforementioned source shifting. As might be expected based on the similarity of the deconvolution maps, the summed region spectra are, to plot resolution, identical when comparing the two propagation models. This extends even to their source rejection capability with the Mach 0.12 data in Fig. 13, where strong non-slat model tones in the wing summation region of Fig. 13a are excluded in an identical fashion in the slat summation region of Fig. 13b. For this test, with the selected deterministic propagation model, and the von Kármán plane wave MCF formulation, it does not appear to matter how the turbulent propagation path details are modeled with regard to source maps and summed spectra (as long as physically reasonable choices are made).

VII. Summary & Recommendations

A means of incorporating turbulence decorrelation effects into microphone phased array analysis has been presented. The method uses existing coherence loss models, with parameters fit to coherence data from in situ speaker measurements, to adjust the modeled CSM used in deconvolution and account for decorrelation. The model fit has the ability to capture the shape and behavior of the coherence data well, as long as the data used in the fit would yield perfect coherence in the absence of turbulent scattering. Deconvolution routines are shown to suffer severe blurring of source distributions when baseline algorithms are used. Incorporating the MCF dramatically improves source localization and restores it to expected behavior.

There is some ambiguity in how to best apply the concept in open-jet wind tunnel testing, so two different ways of modeling the turbulent propagation paths are implemented and compared. While some minor differences between the methods are evident when looking at individual coherence values from the microphone phased array, results are practically identical when looking at both source maps and summed regional spectra output from DAMAS.

Some irregularities in source localization are present in the source maps. These irregularities could be due to the limitations of this implementation of the MCF calculation, as every major assumption in the formulation is violated in this application. However, the limitations of the deterministic propagation model may interfere with the ability to assess possible issues with the turbulence coherence loss model. In general application, it appears that having a more accurate model of the mean shear layer geometry and associated propagation effects is necessary to realize significant

improvement in the deconvolution output. Only then should further improvements to the MCF model, such as more refined source modeling, be pursued.

Acknowledgments

References

[1] Dougherty, R. P., "Turbulent Decorrelation of Aeroacoustic Phased Arrays: Lessons from Atmospheric Science and Astronomy," *9th AIAA/CEAS Aeroacoustics Conference*, AIAA 2003-3200, Hilton Head, South Carolina, 12 – 14 May 2003. doi:https://doi.org/10.2514/6.2003-3200.

[2] Pires, L. S., Dougherty, R. P., and Gerges, S. N. Y., "Predicting Turbulent Decorrelation in Acoustic Phased Array," *50th AIAA Aerospace Sciences Meeting*, AIAA 2012-0387, Nashville, Tennessee, 9 – 12 January 2012. doi:https://doi.org/10.2514/6.2012-387.

[3] Ernst, D., Spehr, C., and Berkefeld, T., "Decorrelation of Acoustic Wave Propagation through the Shear Layer in Open Jet Wind Tunnel," *21st AIAA/CEAS Aeroacoustics Conference*, AIAA 2015-2976, Dallas, Texas, 22 – 26 June 2015. doi: https://doi.org/10.2514/6.2015-2976.

[4] Biesheuvel, J., Tuinstra, M., de Santana, L. D., and Venner, C. H., "Effect of turbulent boundary layer induced coherence loss on beamforming measurements in industrial scale wind tunnel tests," *25th AIAA/CEAS Aeroacoustics Conference*, AIAA 2019-2463, Delft, The Netherlands, 20 – 23 May 2019. doi:https://doi.org/10.2514/6.2019-2463.

[5] Bahr, C. J., Hutcheson, F. V., and Stead, D. J., "Unsteady Propagation and Mean Corrections in Open-Jet and Kevlar® Wind Tunnels," *AIAA Journal*, Vol. 59, No. 11, 2021, pp. 4598 – 4609. doi:https://doi.org/10.2514/1.J060469.

[6] Sanders, M. P. J., Venner, C. H., and de Santana, L. D., "Comparabilitiy of High-Lift Noise Measurements in a Hard-Wall, an Open-Jet and a Hybrid Test Section," *AIAA AVIATION Forum*, AIAA 2021-2252, Virtual Event, 2 – 6 August 2021. doi:https://doi.org/10.2514/6.2021-2252.

[7] Bahr, C. J., "Toward Relating Open- and Closed-Test Section Microphone Phased Array Aeroacoustic Measurements," *AIAA AVIATION Forum*, AIAA 2021-2127, Virtual Event, 2 – 6 August 2021. doi:https://doi.org/10.2514/6.2021-2127.

[8] Lockard, D. P., Turner, T. L., Bahr, C. J., and Hutcheson, F. V., "Overview of Aeroacoustic Testing of the High-Lift Common Research Model," *AIAA AVIATION Forum*, AIAA 2021-2113, Virtual Event, 2 – 6 August 2021. doi:https://doi.org/10.2514/6.2021-2113.

[9] Hutcheson, F. V., Lockard, D. P., and Stead, D. J., "On the Alleviation of Background Noise for the High-Lift Common Research Model Aeroacoustic Test," *28th AIAA/CEAS Aeroacoustics Conference*, Accepted, Southampton, UK, 14 – 17 June 2022.

[10] Humphreys, W. M., Lockard, D. P., and Bahr, C. J., "Phased Array Characterization of Slat Noise Radiation from the High-Lift Common Research Model," *28th AIAA/CEAS Aeroacoustics Conference*, Accepted, Southampton, UK, 14 – 17 June 2022.

[11] Turner, T. L., Mulvaney, J. W., Lockard, D. P., Allen, A. R., and Brynildsen, S. E., "Development of Slat Gap and Slat Cove Filler Treatments for Noise Reduction Assessment on the High Lift Common Research Model in the NASA LaRC 14x22," *28th AIAA/CEAS Aeroacoustics Conference*, Accepted, Southampton, UK, 14 – 17 June 2022.

[12] Lockard, D. P., Choudhari, M. M., and Vatsa, V. N., "Aeroacoustic Simulations of the High-Lift Common Research Model and Validation with Experiment," *28th AIAA/CEAS Aeroacoustics Conference*, Accepted, Southampton, UK, 14 – 17 June 2022.

[13] Brooks, T. F., and Humphreys, W. M., "A deconvolution approach for the mapping of acoustic sources (DAMAS) determined from phased microphone arrays," *Journal of Sound and Vibration*, Vol. 294, 2006, pp. 856 – 879. doi:https://doi.org/10.1016/j.jsv.2005.12.046.

[14] Ostashev, V. E., and Wilson, D. K., "Strength and wave parameters for sound propagation in random media," *The Journal of the Acoustical Society of America*, Vol. 141, No. 3, 2017, pp. 2079 – 2092. doi:http://dx.doi.org/10.1121/1.4978781.

[15] Wilson, D. K., "Performance bounds for acoustic direction-of-arrival arrays operating in atmospheric turbulence," *The Journal of the Acoustical Society of America*, Vol. 103, No. 3, 1998, pp. 1306 – 1319. doi:https://doi.org/10.1121/1.421271.

[16] Bahr, C. J., and Horne, W. C., "Subspace-based background subtraction applied to aeroacoustic wind tunnel testing," *International Journal of Aeroacoustics*, Vol. 16, No. 4 & 5, 2017, pp. 299 – 325. doi:https://doi.org/10.1177/1475472X17718885.

[17] Bahr, C., and Cattafesta, L. N., "Limits of coherence-based aeroacoustic analysis in the presence of distributed sources," *The Journal of the Acoustical Society of America*, Vol. 129, No. 6, 2011, pp. EL248 – EL253. doi:https://doi.org/10.1121/1.3582150.

[18] Amiet, R. K., "Refraction of sound by a shear layer," *Journal of Sound and Vibration*, Vol. 58, No. 4, 1978, pp. 467–482. doi:https://doi.org/10.1016/0022-460X(78)90353-X.

[19] Ostashev, V. E., and Wilson, D. K., "Line-of-sight sound propagation in a random moving medium," *Acoustics in Moving Inhomogeneous Media*, CRC Press, 2016, 2nd ed.

[20] Humphreys, W. M., Brooks, T. F., Bahr, C. J., Spalt, T. B., Bartram, S. M., and Culliton, W. G., "Development of A Microphone Phased Array Capability for the Langley 14- by 22-Foot Subsonic Tunnel," *20th AIAA/CEAS Aeroacoustics Conference*, AIAA 2014-2343, Atlanta, Georgia, 16 – 20 June 2014. doi:https://doi.org/10.2514/6.2014-2343.

[21] Sarradj, E., "Three-Dimensional Acoustic Source Mapping with Different Beamforming Steering Vector Formulations," *Advances in Acoustics and Vibration*, Vol. 2012, No. 292695, 2012, pp. 1 – 12. doi:https://doi.org/10.1155/2012/292695.

[22] Bahr, C. J., and Lockard, D. P., "Designing Shading Schemes for Microphone Phased Arrays," *8th Berlin Beamforming Conference*, BeBeC-2020-S1, Berlin, Germany, 2 – 3 March 2020.

[23] *Method for Calculation of the Absorption of Sound by the Atmosphere*, ANSI S1.26-1995 (ASA 113-1995), Acoustical Society of America, 1995.

[24] Bahr, C. J., Brooks, T. F., Humphreys, W. M., Spalt, T. B., and Stead, D. J., "Acoustic Data Processing and Transient Signal Analysis for the Hybrid Wing Body 14- by 22-Foot Subsonic Wind Tunnel Test," *20th AIAA/CEAS Aeroacoustics Conference*, AIAA 2014-2345, Atlanta, Georgia, 16 – 20 June 2014. doi:https://doi.org/10.2514/6.2014-2345.

[25] Jiao, J., Delfs, J. W., and Dierke, J., "Toward CAA based Acoustic Wind Tunnel Corrections for Realistic Shear Layers," *21st AIAA/CEAS Aeroacoustics Conference*, AIAA 2015-3278, Dallas, Texas, 22 – 26 June 2015. doi:https://doi.org/10.2514/6.2015-3278.

[26] Biesheuvel, J., Tuinstra, M., de Santana, L. D., and Venner, C. H., "Finite thickness effects and corrections for acoustic waves propagating through shear layers," *AIAA AVIATION Forum*, AIAA 2021-2130, Virtual Event, 2 – 6 August 2021. doi:https://doi.org/10.2514/6.2021-2130.

(a) 5 kHz, baseline DAMAS

(b) 20 kHz, baseline DAMAS

(c) 5 kHz, array center model

(d) 20 kHz, array center model

(e) 5 kHz, pair-by-pair model
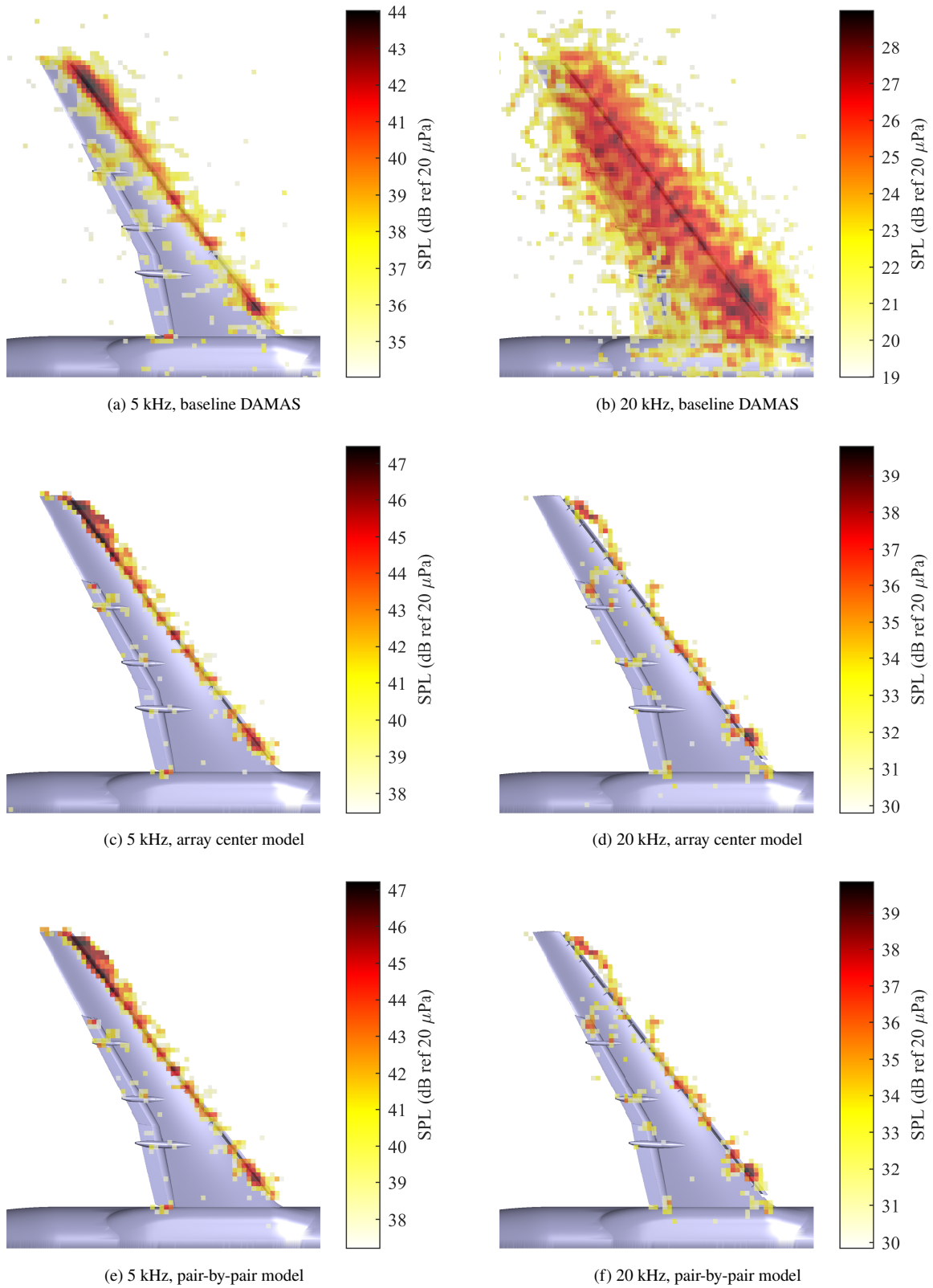
(f) 20 kHz, pair-by-pair model

Fig. 7   Comparison of noise source maps between the baseline DAMAS algorithm and the two considered propagation models at 5 kHz and 20 kHz. Results are for Mach 0.16 at the 90° array station and 8.5° angle of attack.
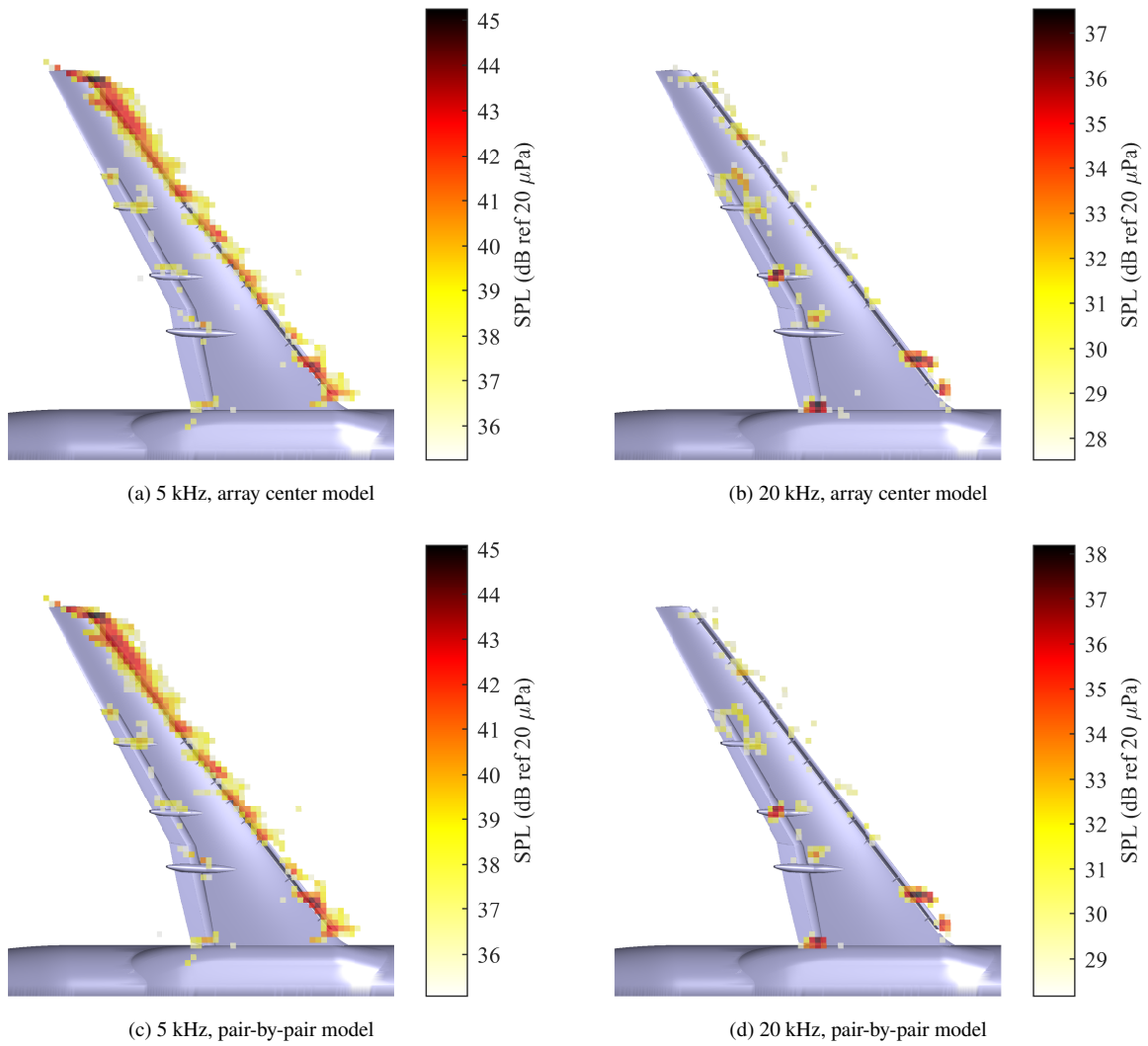
(a) 5 kHz, array center model

(b) 20 kHz, array center model

(c) 5 kHz, pair-by-pair model

(d) 20 kHz, pair-by-pair model

Fig. 8   Noise source maps for the two considered propagation models at 5 kHz and 20 kHz. Results are for Mach 0.16 at the 70° array station and 8.5° angle of attack.
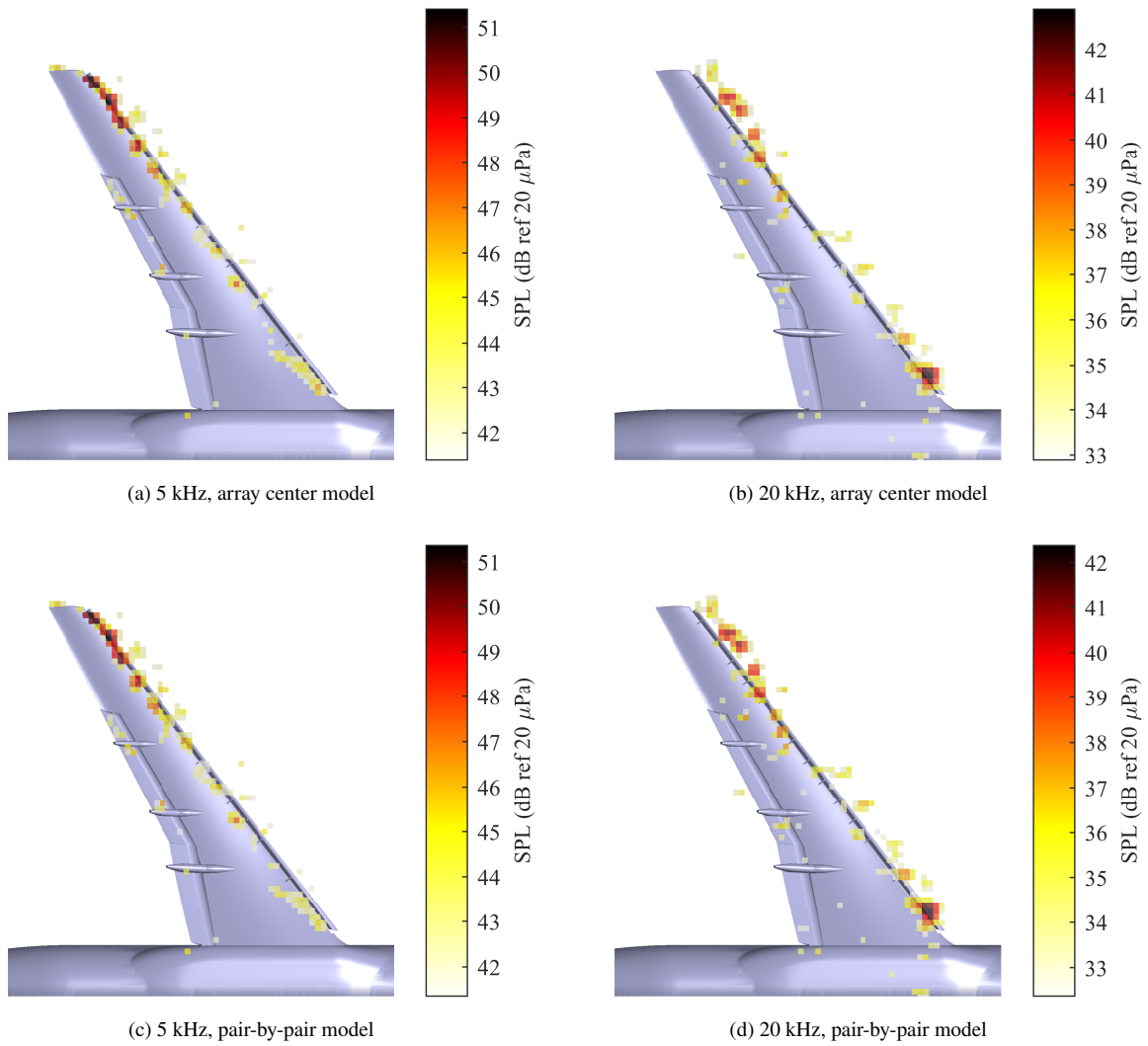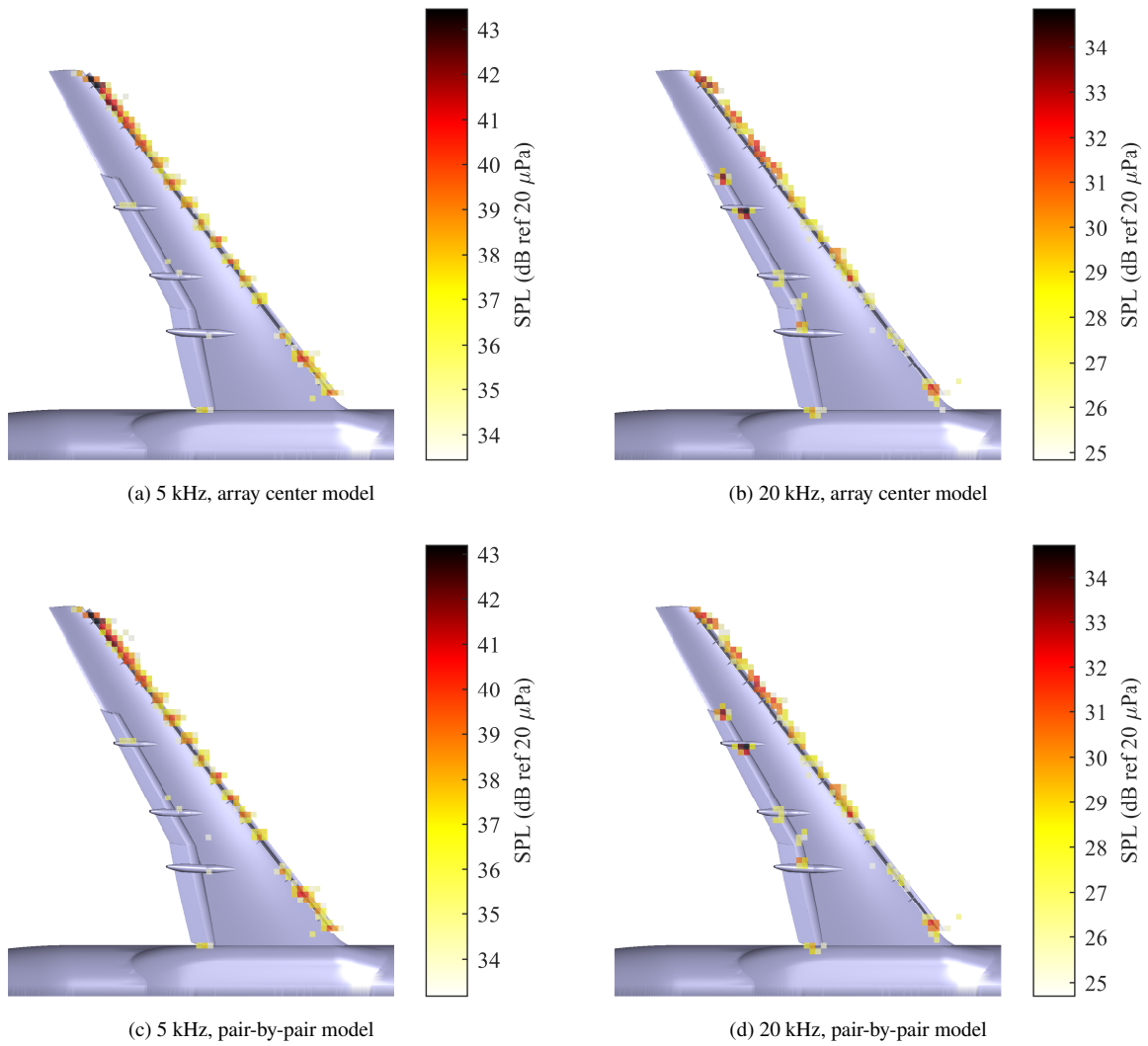
(a) 5 kHz, array center model

(b) 20 kHz, array center model

(c) 5 kHz, pair-by-pair model

(d) 20 kHz, pair-by-pair model

Fig. 9   Noise source maps for the two considered propagation models at 5 kHz and 20 kHz. Results are for Mach 0.16 at the 110° array station and 8.5° angle of attack.
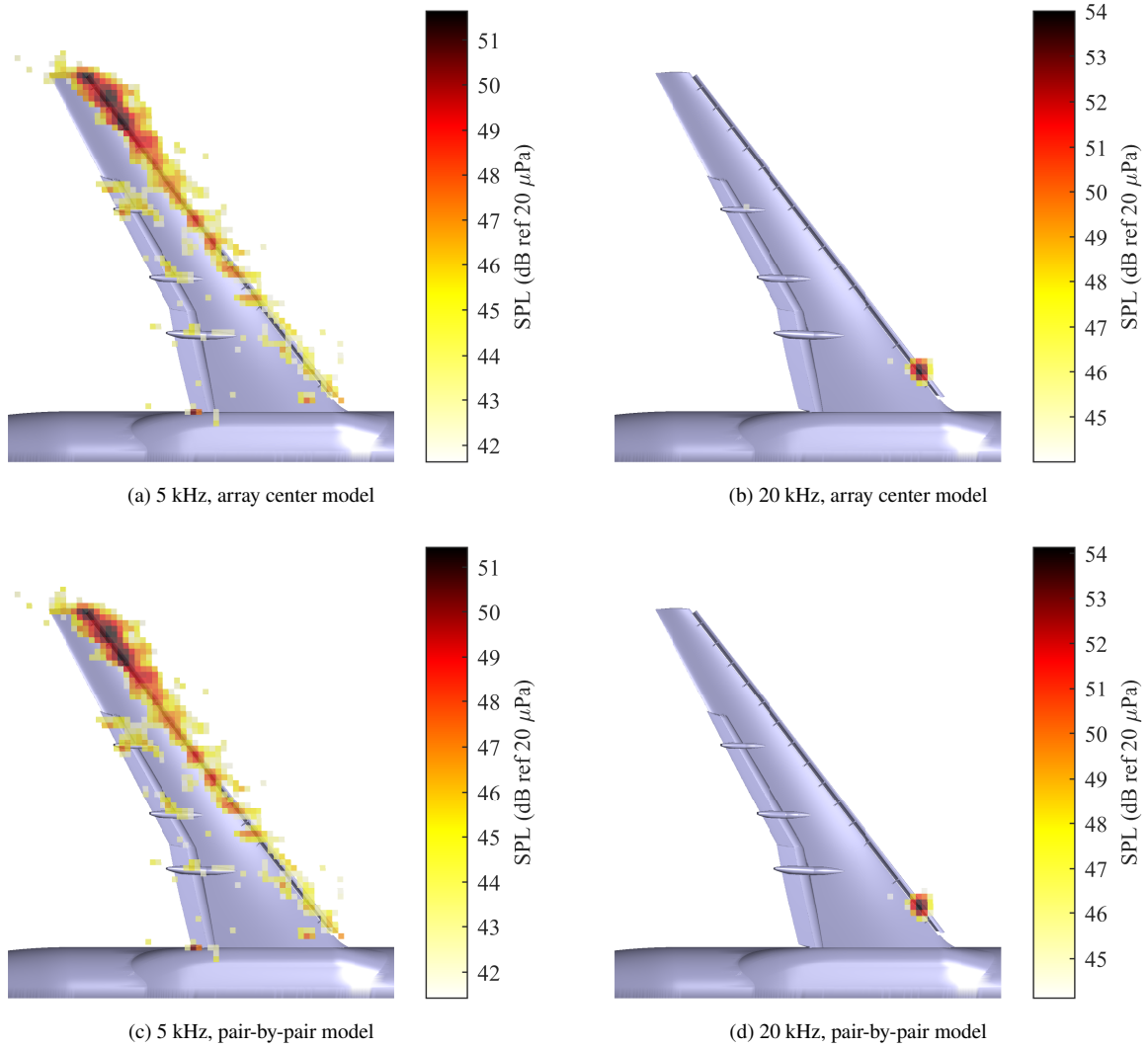
(a) 5 kHz, array center model

(b) 20 kHz, array center model

(c) 5 kHz, pair-by-pair model

(d) 20 kHz, pair-by-pair model

Fig. 10   Noise source maps for the two considered propagation models at 5 kHz and 20 kHz. Results are for Mach 0.12 at the 90° array station and 8.5° angle of attack.
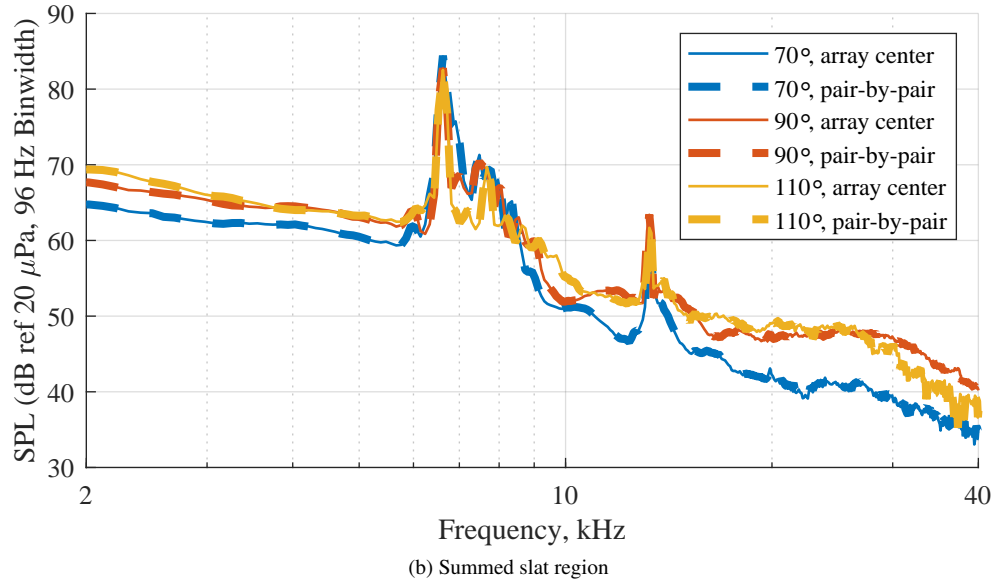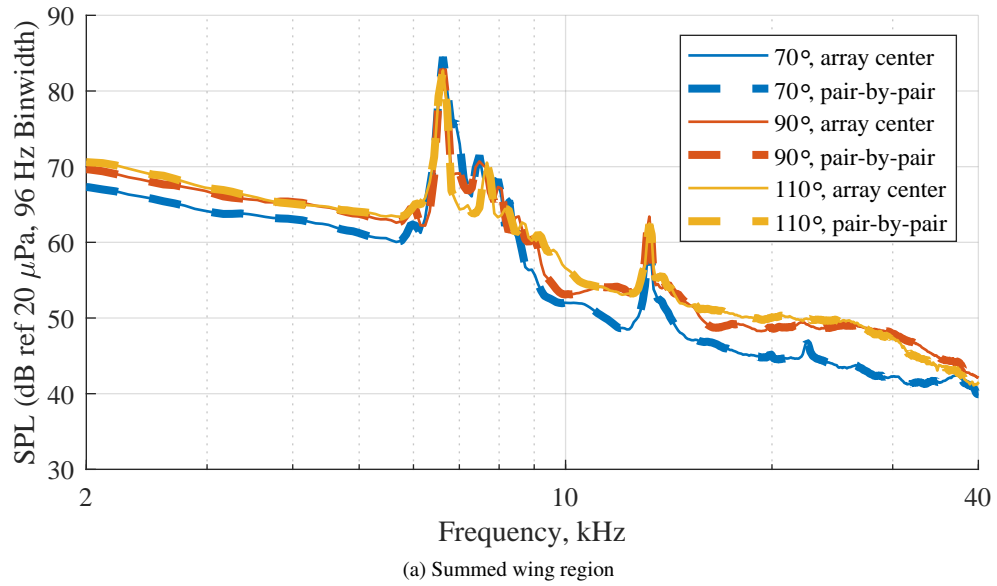
(a) 5 kHz, array center model

(b) 20 kHz, array center model

(c) 5 kHz, pair-by-pair model

(d) 20 kHz, pair-by-pair model

Fig. 11   Noise source maps for the two considered propagation models at 5 kHz and 20 kHz. Results are for Mach 0.20 at the 90° array station and 8.5° angle of attack.

(a) Summed wing region

(b) Summed slat region

Fig. 12 Comparison of summed source region narrowband spectra as a function of measurement station at Mach 0.16 and 8.5° angle of attack.

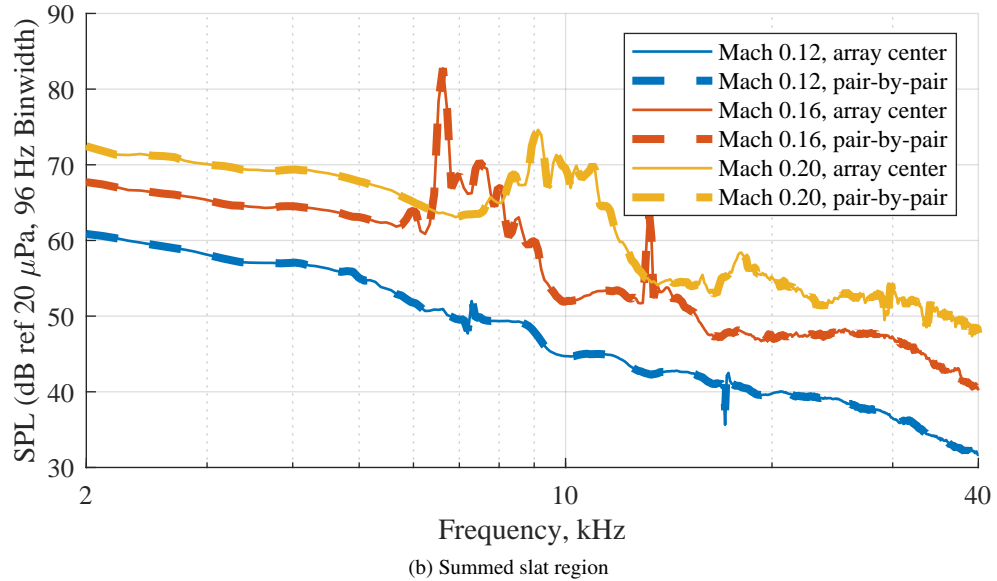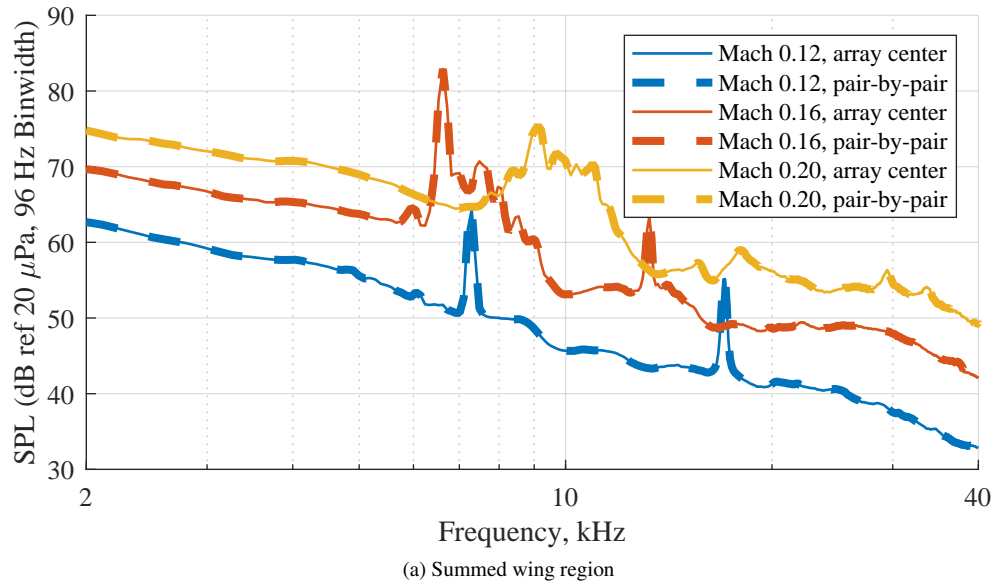(a) Summed wing region

(b) Summed slat region

Fig. 13   Comparison of summed source region narrowband spectra as a function of Mach number at the 90°
array station and 8.5° angle of attack.